Check for updates

steel research international

steel research international

RESEARCH ARTICLE OPEN ACCESS

Fatigue Strength in Additive Toolmaking: A Study of Metal Binder Jetting and Electron Beam Melting for Processing Carbide-Rich Cold-Work Tool Steels

Frederik Tegeder[1] | Lennart Mirko Scholl[1] | Sandra Wieland[2] | Christian Weck[2] | Marie Franke-Jurisch[3] | Alexander Bezold[1] | Thomas Weißgärber[2,3] | Christoph Broeckmann[1]

[1]Institute for Materials Applications in Mechanical Engineering (IWM), RWTH Aachen University, Aachen, Germany | [2]Fraunhofer Institute for Manufacturing Technology and Applied Materials Research (IFAM), Bremen, Germany | [3]Fraunhofer Institute for Manufacturing Technology and Applied Materials Research (IFAM), Dresden, Germany

Correspondence: Frederik Tegeder (f.tegeder@iwm.rwth-aachen.de)

Received: 30 June 2025 | **Revised:** 5 March 2026 | **Accepted:** 11 March 2026

Keywords: A11/V10 PM | additive manufacturing | carbide-rich tool steels | critical defect sizes | electron beam melting | HCF strength | metal binder jetting

ABSTRACT

Additive manufacturing (AM) offers numerous possibilities for toolmaking, such as the integration of internal cooling structures, easy fabrication of complex tool geometries, or hybrid manufacturing. Another important aspect is the minimization of necessary post-processing steps through near-net-shape manufacturing, which enables needed cost and effort savings, especially for difficult-to-machine, carbide-rich tool steels. Previous studies have investigated laser powder bed fusion (PBF-LB/M) as a possible process. However, PBF-LB/M is not applicable to all steels. In this study, AISI A11 was successfully processed using metal binder jetting and electron beam melting both with optional hot isostatic pressing (HIP). The resulting microstructures were characterized depending on the AM process. Mechanical investigations enable appropriate microstructure–property correlations for fatigue performances. For additively manufactured A11, the high cycle fatigue (HCF, $N_G = 10^7$) strengths are statistically evaluated under rotation bending tests. Those results are compared to conventional A11 PM produced via HIP and subsequent hot working. The results show that AM toolmaking of high vanadium alloyed, carbide-rich tool steels is a promising alternative to conventional steelmaking.

1 | Introduction

Tooling costs and setup times represent a significant cost factor in massive cold forming applications. Enhancing tool lifetimes and increasing production volumes per tool while minimizing retooling times is of great economic interest to establish more resource-efficient and low-emission fabrication chains. Particularly crucial is the wear resistance of carbide-rich cold-work tool steels (CWS), which can be improved by increasing carbide content and hardness.

As tool life increases due to improved wear resistance, however, the fatigue performance becomes the overall determining factor for tool longevity. Reiss [1], Jung [2] and Jesner [3] report that most tools used in cold (bulk) metal forming of complex shaped components fail due to fatigue fracture. Nowadays, additive manufacturing (AM) technologies are increasingly used in various industries. Providing unparalleled geometric flexibility and opening up new possibilities for innovative manufacturing, component design and functional integrations. Potential future applications for AM tools made from CWS (like A11) include wear-resistant stamping, embossing, and full-forward pressing tools as well as rollers or extruder screws.

Typical AM processes can be categorized into beam-based (e.g., laser or electron) and sinter-based techniques [4–6]. Especially for the tooling sector, AM presents numerous advantages to

This is an open access article under the terms of the Creative Commons Attribution License, which permits use, distribution and reproduction in any medium, provided the original work is properly cited.

© 2026 The Author(s). *steel research international* published by Wiley-VCH GmbH.

extend tool performances and lifetimes by integrating internal cooling channels or structures [7], hybrid manufacturing or optimizing tool design [4]. The expanded construction and alloying freedom in AM processes enables focusing on the three key optimization goals for industrial metal cold forming tools: process efficiency, sustainability, and performance enhancements [5–7].

For establishing AM tools as viable alternatives in tooling applications, it is essential to understand the relationships within the process–structure–property–performance (PSPP) chain, e.g., correlations between process parameters, resulting microstructures and mechanical properties.

Besides microstructural and mechanical characterization, the achievable AM tool performance has to be benchmarked against established conventional steelmaking/toolmaking.

In recent years, AM of hard, high-alloyed steels like AISI H13, M50, and M2 has been intensively investigated [8–11], whereby Kunz et al. [9–11] and also Kempen et al. [12] showed processibility for those steels via PBF-LB/M. But in many cases [8–13], the fatigue strength without (and even with) hot isostatic pressing (HIP) is clearly reduced compared to conventional steelmaking. Kunz et al. [9] report that high speed steel (HSS) such as 1.3244/2 show poor or no processibility with PBF-LB/M due to locally high cooling rates and strong temperature gradients [8–13]. CWS with high C, Co, or V contents like A11 exhibit high hot cracking tendencies and residual stresses (RS), and thus, up to date, are only partially or not processable via laser-based AM methods.

Alternatively, Godlinski et al. [14] showed that complex shaped tool inserts with internal structures made of M2 and X190CrVMo20 can be processed via binder-based 3D-printing. Metal binder Jetting (MBJ) offers promising solutions for the mentioned hot cracking phenomena. During MBJ, the steel powder is not melted. Instead, green parts are formed in powder beds by depositing organic binders with subsequent consolidation through sintering (SI) in a furnace [14–17].

Furthermore, electron beam melting (EBM) shows the potential for processing CWS like A11 due to its lower cooling rates and reduced thermal gradients compared to PBF-LB/M [18]. A thorough understanding of process parameter influences from MBJ and EBM on microstructure, and intrinsic defect populations is important to elucidate the PSPP relationships. The suitability of both MBJ and EBM techniques for near-net-shape AM processing of CWS, particularly the resulting microstructure, fatigue strength, and crack-initiation mechanisms, has not yet been studied in the literature so far.

Closing this gap, the present work focuses on AM processing A11 using MBJ and EBM, followed by a systematic characterization within the PSPP framework. The aim is to profoundly understand the manufacturing influences on steel microstructure and fatigue performance. Therefore, a complete statistical evaluation of manufacturing-related, crack-initiating defects is performed for various A11 grades, creating a fatigue and defect database. The AM techniques are benchmarked against three different conventional A11 PM + HIP steels, whereby PSPP correlations are developed based on the evaluated database.

2 | Materials, Methods, and Experimental Procedures

Different raw materials from the ledeburitic, carbide-rich tool steel AISI A11 (X245VCrMo10-5-1/V10) fabricated by PM + HIP were provided as pre-peeled round bars or pre-milled square blocks in hot worked and soft-annealed conditions by the industrial manufacturer DEW GmbH (V10 PM^1, as blocks with: $\approx$ 320 mm $\times$ 320 mm $\times$ 700 mm, $\varphi \approx 0.7$) and ZAPP Precision Metals GmbH (V10 PM^2, Erasteel SAS, as rods with: Ø $\approx$ 58,0 mm, $\varphi \approx 2.0$, and V10 PM^3, voestalpine Böhler Edelstahl GmbH, as rods with Ø $\approx$ 13,1 mm, $\varphi \approx 6.0$). A11 grade powders with different particle size distributions for AM were provided by DEW GmbH.

The chemical compositions of raw materials or steel powders determined using optical emission spectroscopy (OES) are presented in Table 1. It can be noticed that the C and V contents of the A11 grades exhibit stronger variability. Both MBJ and EBM samples show increased C and V contents. Stronger increased C contents of both MBJ samples can be attributed to the organic binder (during curing probably not fully outgassed). Also, the EBM-Z samples without HIP display a slightly elevated C content. For PM-L^1/-T^{1,} a slightly increased S content is noted (see footnotes, higher sulfurization facilitates steel machining due to increased MnS content).

TABLE 1 | Chemical composition (wt%) of the investigated steels (obtained by OES, balance Fe).

Steel	Chemical composition, wt% obtained by OES									
A11/V10	C	V	Cr	Mo	Si	P	S	Co	Ni	Mn
EBM-Z	2.66	10.64	4.87	1.25	0.85	0.03	0.02	0.07	0.13	0.64
EBM-Z + HIP	2.57	10.75	4.88	1.27	0.87	0.03	0.02	0.07	0.12	0.63
MBJ-Z	2.71	10.85	5.24	1.35	0.89	0.03	0.02	0.08	0.14	1.05
MBJ-Z + HIP	2.70	10.20	5.35	1.31	0.88	0.03	0.02	0.08	0.15	1.06
PM-L1/-T^{1a}	2.52	9.39	5.59	1.29	1.06	0.04	0.10	0.06	0.08	0.53
PM-L^{2b}	2.56	10.18	5.52	1.14	0.75	0.03	0.07	0.06	0.08	0.50
PM-L^{3c}	2.36	9.85	4.75	1.12	0.79	0.03	0.05	0.03	0.15	0.47

[a]V10 PM-L^1/-T^1: Targeted steel manufacturing with increased sulfurization (S content), intentional decreased steel/melt cleanliness during powder atomization and reduced hot working degree ($\varphi \approx 0.7$).
[b]V10 PM-L^2: Standard sulfurization (S content), standard steel/melt cleanliness and handling during pow- der atomization, typical hot working degree ($\varphi \approx 2.0$) used in industrial fabrications.
[c]V10 PM-L^3: Enhanced steel manufacturing with very high steel/melt cleanliness and strongly increased hot working degree ($\varphi \approx 6.0$).

1869344x, 0, Downloaded from https://onlinelibrary.wiley.com/doi/10.1002/srin.202500658 by Universitatsbibliothek RWTH Aachen University, Wiley Online Library on [08/05/2026]. See the Terms and Conditions (https://onlinelibrary.wiley.com/terms-and-conditions) on Wiley Online Library for rules of use; OA articles are governed by the applicable Creative Commons License

Both EBM batches show doubled Mn content compared to the conventional A11 PM + HIP grades (Mn enhances hardenability). Besides C, the relevant alloying elements necessary for carbide formation are V, Cr, and Mo, which together define the achievable carbide content inside the steel. Cr and Mo contents are within a consistent range across all different A11 grades. The A11 microstructures are depicted in Figure 1 as light optical micrographs of fatigue samples in heat treated and etched conditions (V2A etchant: HNO3 + C2H5OH + HCl · H_2O). All eight different A11 batches exhibit a fully martensitic matrix (brown) with smaller or larger, finely dispersed primary vanadium carbides (MC/VC, white). Notably, the achieved carbide structures (size, shapes, spatial distribution, coarsening and clustering phenomena) shown in Figure 1 differ depending on the applied manufacturing technique; particularly, the PM samples appear to have finer and more uniformly distributed carbides Figure 1c,d,g,h.

To provide a comprehensive overview of the A11 batches, Table 2 summarizes the key information related to the steelmaking processes, powder characteristics, and manufacturing parameters.

EBM-Z and EBM-Z + HIP microstructures show very small, roundly shaped MC carbides with homogeneous distributions and sometimes stronger coarsened single MC or smaller coarsened MC clusters (see Figure 1a,e). The conventional grades PM-L^1/-T^1, PM-$L^{2,}$ and PM-L^3 obtain a highly homogeneous carbide structure with very small, spheroidal shaped MC, despite different HW degrees φ seem quite similar to each other and carbide coarsening or clustering is rarely found in microscopic observations (see Figure 1c,d,g,h). In contrast, MBJ-Z and MBJ-Z + HIP microstructures exhibit a strong coarsening of carbide structures/most MC single carbides with sometimes MC clustering (see Figure 1b,f).

To focus more on microstructural differences between both applied AM techniques, Figures 2 and 3 exemplarily illustrates different MC coarsening/clustering and volume defects found for A11 EBM-Z and A11 MBJ-Z fabricated samples. EBM generates larger single pores (see Figure 3a bottom) or (smaller) grouped pores (see Figure 3b bottom) as well as sometimes coarsened MC clusters (see Figure 3a,b top). Applying HIP after EBM seems to close those porosities completely, thus only coarsened MC single carbides or clusters remain as conspicuous microstructural discontinuities (see Figures 2a and 3d,e). MBJ creates single or grouped micro cavities (see Figure 3c) and after sintering appears a throughout strongly coarsened primary MC carbide structure, which seems unchanged and not further influenced by HIP (see Figures 2b and 3f). Similar to EBM, the porosities inside the MBJ-Z + SI microstructure seem to vanish completely after applying HIP (see Figure 3f). For all eight A11 batches, Table 2 provides relevant information regarding steelmaking,

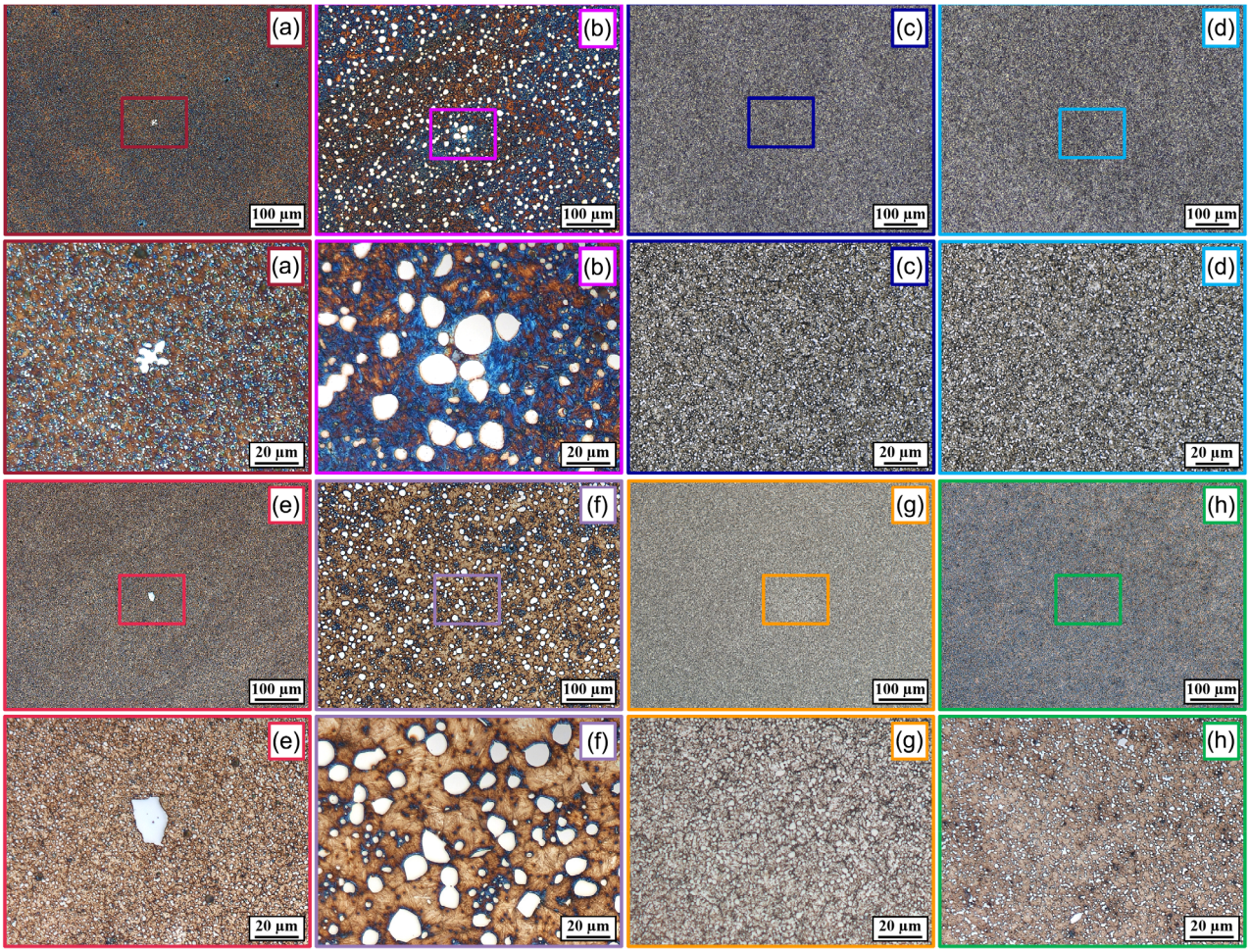


FIGURE 1 | V2A-etched microstructures of the investigated A11 steels (boxes mark enlarged areas): (a) EBM-Z, (b) MBJ-Z, (c) PM-L^1, (d) PM-T^1, (e) EBM-Z + HIP, (f) MBJ-Z + HIP, (g) PM-L^2, and (h) PM-L^3.

1869344x, 0, Downloaded from https://onlinelibrary.wiley.com/doi/10.1002/srin.202500658 by Universitatsbibliothek RWTH Aachen University, Wiley Online Library on [08/05/2026]. See the Terms and Conditions (https://onlinelibrary.wiley.com/terms-and-conditions) on Wiley Online Library for rules of use; OA articles are governed by the applicable Creative Commons License

TABLE 2 | Information regarding used steel and additive manufacturing processes, powder size distributions, and printing machines as well as curing/debinding, sintering, density and hot working (HW) parameters.

Steel A11/V10	Powder D_{50}, µm	Printing/fabrication [-]	Curing ($T_C/t_C \approx \ldots$ / atmosphere)	Sintering (SI) ($T_S/t_S \approx \ldots$ / atmosphere)	Rel. density [-]	Hot working (HW) Degree $\varphi \approx \ldots$ [-]	Hot working (HW) Type [-]
EBM-Z	≈ 90–100	Arcam A2X	—	—	0.998	—	—
EBM-Z + HIP			—	—	1.0	—	—
MBJ-Z	≈ 20–30	ExOne Innovent+	180°C/ 60 min /Argon 5.0	1260°C/60 min /Vacuum	0.983	—	—
MBJ-Z + HIP					1.0	—	—
PM-L[1]/-T1[a]	≈ 80–100	PM + HIP + Forging	—	—	1.0	0.7	Open-die
PM-L2[b]	≈ 90–110		—	—	1.0	2.0	Round
PM-L3[c]	≈ 100–120		—	—	1.0	6.0	Round

[a]V10 PM-L[1]/-T[1]: Targeted steel manufacturing with increased sulfurization (S content), intentional decreased steel/melt cleanliness during powder atomization, and reduced hot working degree ($\varphi \approx 0.7$).
[b]V10 PM-L[2]: Standard sulfurization (S content), standard steel/melt cleanliness and handling during powder atomization, typical hot working degree ($\varphi \approx 2.0$) used in industrial fabrications.
[c]V10 PM-L[3]: Enhanced steel manufacturing with very high steel/melt cleanliness and strongly increased hot working degree ($\varphi \approx 6.0$).

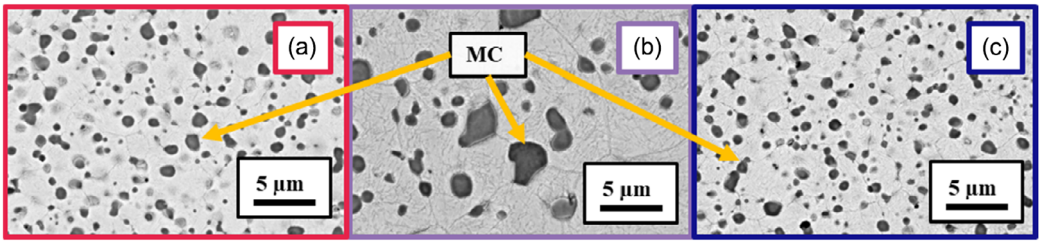


FIGURE 2 | SEM image of the microstructure, captured using a CBS detector: (a) EBM-Z + HIP, (b) MBJ-Z + HIP, (c) PM-L[1].

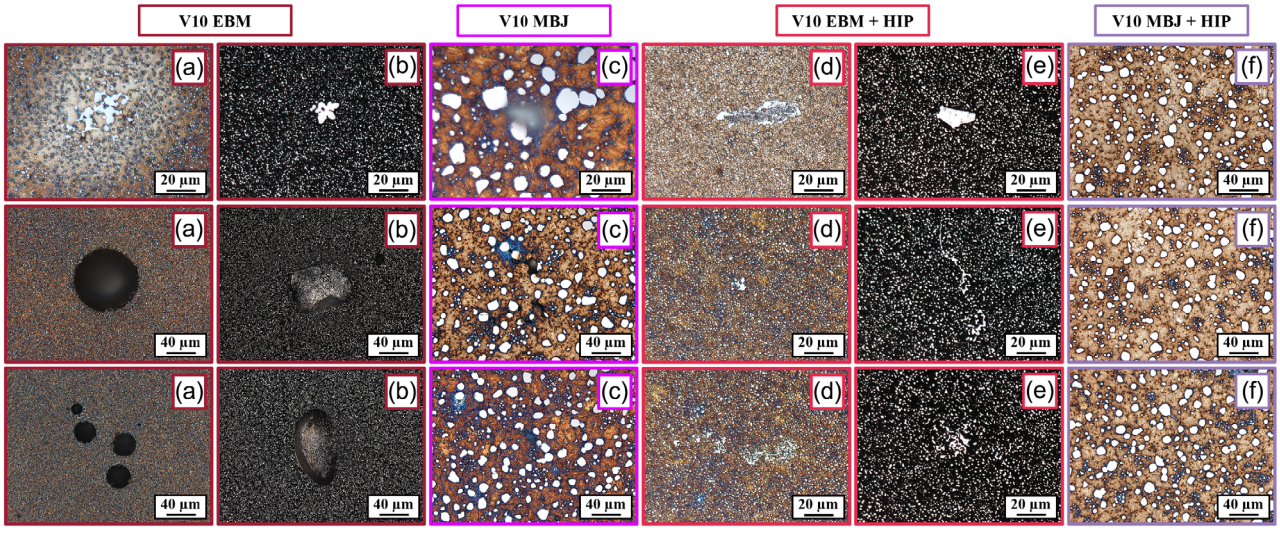


FIGURE 3 | Manufacturing-related MC coarsening and volume defects in A11: etched with V2A at (a) RT and (b) 70°C for EBM-Z, (c) RT for MBJ-Z, (d) RT and (e) 70°C for EBM-Z + HIP, (f) RT for MBJ-Z + HIP.

powder, manufacturing processes, and HW. Acc Franke-Jurisch et al. [18] the A11 EBM-Z samples were built at $T_{EBM} \approx 850$°C using a cross-snake scan strategy with 70 µm layer thickness, a 50 µm line offset and an area energy $E_{Area} \approx 4.0$ J/mm^2.

Acc Tegeder et al. [19] the A11 MBJ-Z samples were printed with a 40 µm layer thickness (standard organic water-based binder, 65% binder saturation) and a 30 mm/s traverse roller speed. After MBJ, subsequent curing of the organic binder and SI is applied with the parameters given in Table 2. All AM samples were built as small cylinders in Z direction ($Ø_{EBM} \approx 13$ mm, $Ø_{MBJ} \approx 11$ mm) and are designated as EBM-Z or MBJ-Z (center axis parallel to Z). Small blank cylinders or blocks from conventional A11 raw materials were fabricated in longitudinal (L) and exceptional for PM-T[1] also in transversal (T) direction by sawing

1869344x, 0, Downloaded from https://onlinelibrary.wiley.com/doi/10.1002/srin.202500658 by Universitatsbibliothek RWTH Aachen University, Wiley Online Library on [08/05/2026]. See the Terms and Conditions (https://onlinelibrary.wiley.com/terms-and-conditions) on Wiley Online Library for rules of use; OA articles are governed by the applicable Creative Commons License

TABLE 3 | Heat treatment (HT) parameters, target and achieved hardnesses of the corresponding RBT fatigue specimens from all steels (vacuum furnace with high-pressure nitrogen gas quenching at ≈ 5–8 bar).

Steel A11	Target hardness, HRC	Austenitizing ($T_A \approx .../t_A \approx ...$)	Tempering ($T_T \approx .../t_T \approx ...$)	Achieved hardness [HRC]
EBM-Z	59–60	1180–1190°C/15 min	570°C/3 x 2.0 h	59.8 ± 0.5
EBM-Z + HIP				59.4 ± 0.5
MBJ-Z			560°C/3 x 2.0 h	59.5 ± 0.5
MBJ-Z + HIP				59.7 ± 0.6
PM + HIP-L^1/-T^1			570°C/3 x 2.0 h	59.2 ± 0.4/59.4 ± 0.5
PM + HIP-L^2				59.7 ± 0.6
PM + HIP-L^3				59.6 ± 0.6

(blocks) or wire eroding (rods). All blank cylinders/blocks were subsequently soft turned on a CNC lathe with solid carbide inserts to oversized fatigue specimens (0.5–1.0 mm oversize, compare to Figure 4).

Using HT parameters specified in Table 3, all oversized fatigue samples were industrially heat treated (hardening + tempering) at Dörrenberg Edelstahl GmbH (PM-L^1/-T^1, PM-L^2, PM-L^3), Bodycote Wärmebehandlung GmbH (EBM), and Kutz & Schulze Härterei GmbH (MBJ). Using TiN-coated CBN tools, the fatigue samples were hard turned to final dimensions depicted in Figure 4. Surface finishing was performed at OTEC Präzisionsfinish GmbH using dry drag finishing in coated granulates resulting in mirror-like, low roughness surfaces ($R_z < 0.9$).

Rotating bending tests (RBT) were conducted acc DIN 50 113 [20] on Rapid PUNN test machines (Carl Schenck AG) at $R = -1/f_{RBT}$ ≈ 100–115 Hz. Acc DIN 50 100 [21] long life fatigue (LLF) regime was determined using staircase and short life fatigue (SLF) regime using horizon method. Fatigue data was statistically evaluated acc [21] using in-house software SAFD 5. Gaussian distribution with Rossow estimation function, sample weighting and combination method for LLF was applied. SLF was determined via pearl string method.

Both fracture surfaces of each fatigue specimen were analyzed as illustrated in Figure 5 using a JEOL-JSM 6500 scanning electron microscope (SEM) equipped with secondary (SE) and backscattered electron (BSE) detectors and energy-dispersive X-ray spectroscopy (EDS).

Figure 5 exemplarily shows the SFSA workflow for each A11 grade. The geometrical properties (e.g., area, shape factors, and perimeter) of each crack-forming defect are determined according to the SFSA method established by Scholl et al. [22–26].

Chemical compositions of the critical defects are obtained from EDS. The SFSA enables systematic characterizations and comparisons of different critical defects. Representative EDS spectra of the analyzed critical defects for all investigated A11 grades and processing routes are provided in the Supporting Information (Figures S1–S11). Furthermore, it provides for all A11 grades and regardless of the analyzed defect type the application of Murakami's fatigue model [13, 27] and the development of "normalized" S-N curves [13, 27].

3 | Results

The individual RBT results of A11 grades are presented in Figure 6 as 'standard' S-N curves with a fit line for $\sigma_{A,P=50\%}$ (failure probability $p = 50\%$). Filled circles represent run outs (numbers behind the circles indicate amount per stress level), hollow circles indicate direct fractures and hollow triangles denote upstaired fractures on run-outs.

Table 4 provides the statistically evaluated fatigue strengths $\sigma_{A,P=1-99\%}$ (failure probability ranging from $p = 1\%$ to 99%) and associated scatter bands for LLF regime. The results shown in Table 4 and Figure 6 clearly demonstrate that the manufacturing technique has a significant impact on LLF performances.

EBM-Z and MBJ-Z without HIP exhibit the overall lowest LLF strengths and EBM-Z the largest relative scatter band (see Table 4 and Figure 6). Conventional PM-L^1 and PM-T^1 grades

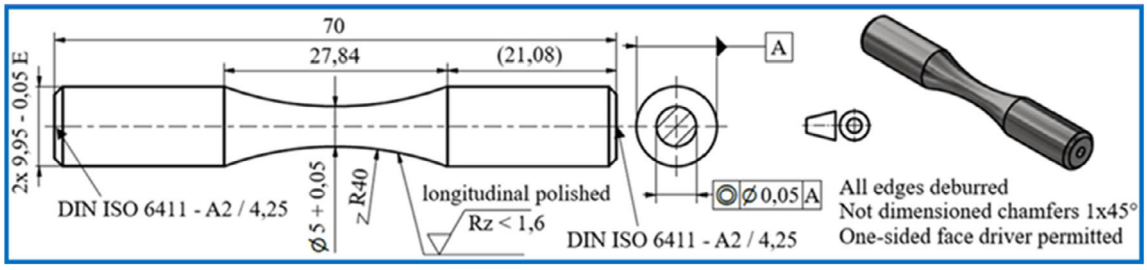


FIGURE 4 | Final specimen geometry after HT, hard turning and surface finishing used for RBT of all A11 steels (due to height limitations of the Arcam A2X printer building room, fatigue specimens from MBJ-Z and MBJ-Z + HIP have reduced head lengths of ca. 13.5 mm compared to 21.08 shown here, otherwise same geometry/test area in the specimen center, as long as the heads can be clamped inside the fatigue testing machine the head lengths are irrelevant for the fatigue test results).

1869344x, 0, Downloaded from https://onlinelibrary.wiley.com/doi/10.1002/srin.202500658 by Universitatsbibliothek RWTH Aachen University, Wiley Online Library on [08/05/2026]. See the Terms and Conditions (https://onlinelibrary.wiley.com/terms-and-conditions) on Wiley Online Library for rules of use; OA articles are governed by the applicable Creative Commons License

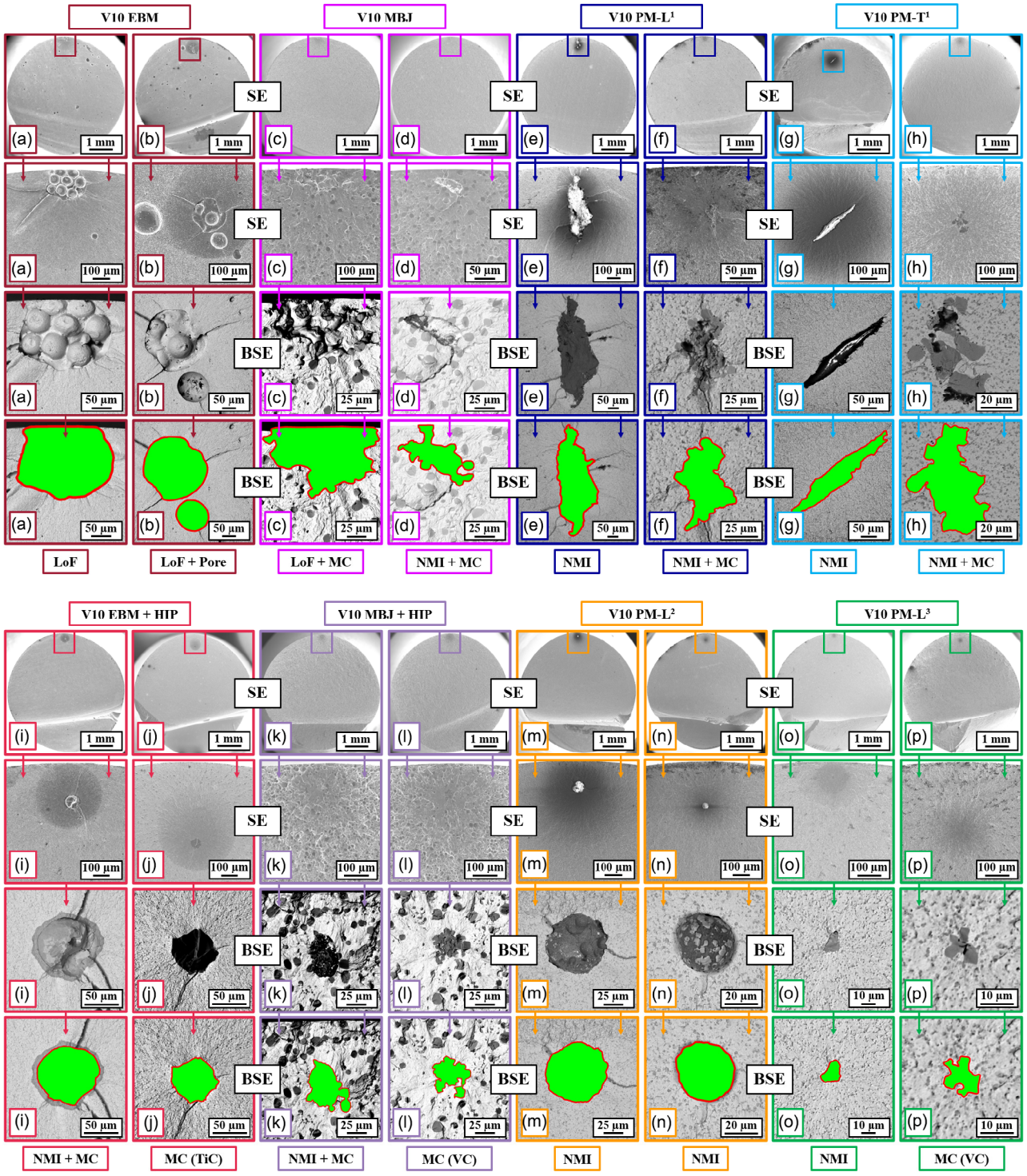


FIGURE 5 | Statistical fracture surface analysis (SFSA) acc Scholl et al. [22–26] applied on various A11 tool steels to create and evaluate a critical defect database: (a + b) EBM-Z, (c + d) MBJ-Z, (e + f) PM-L^1, (g + h) PM-T^1, (i + j) EBM-Z + HIP, (k + l) MBJ-Z + HIP, (m + n) PM-L^2, and (o + p) PM-L^3.

with the lowest cleanliness and HW degree ($\varphi \approx 0.7$) achieve higher $\sigma_{A,P=50\%}$ than both AM steels without HIP. Applying HIP on both AM grades significantly improves the LLF strengths, shifting $\sigma_{A,P=50\%}$ for MBJ-Z + HIP and EBM-Z + HIP above PM-L^1/-T^1 level. Even higher $\sigma_{A,P=50\%}$ values are achieved by the conventional A11 grades PM-L^2 and PM-L^3. The overall highest $\sigma_{A,P=50\%}$ is obtained by PM-L^3, which is manufactured with highest cleanliness, HW degree φ. The different fatigue results can be effectively explained using SFSA results (see Figures 4, 7 and 8). Under fatigue loading, the most crucial (equal critical) defects inside the volume or at the surfaces are activated inside A11 microstructures and lead to crack initiation (defect-based fatigue mechanisms).

Depending on powder and manufacturing different defect types/sizes are found: for EBM-Z large lack of fusion (LoF) and pores (see Figure 5a,b), for MBJ-Z single/grouped micro cavities or

1869344x, 0, Downloaded from https://onlinelibrary.wiley.com/doi/10.1002/srin.202500658 by Universitatsbibliothek RWTH Aachen University, Wiley Online Library on [08/05/2026]. See the Terms and Conditions (https://onlinelibrary.wiley.com/terms-and-conditions) on Wiley Online Library for rules of use; OA articles are governed by the applicable Creative Commons License

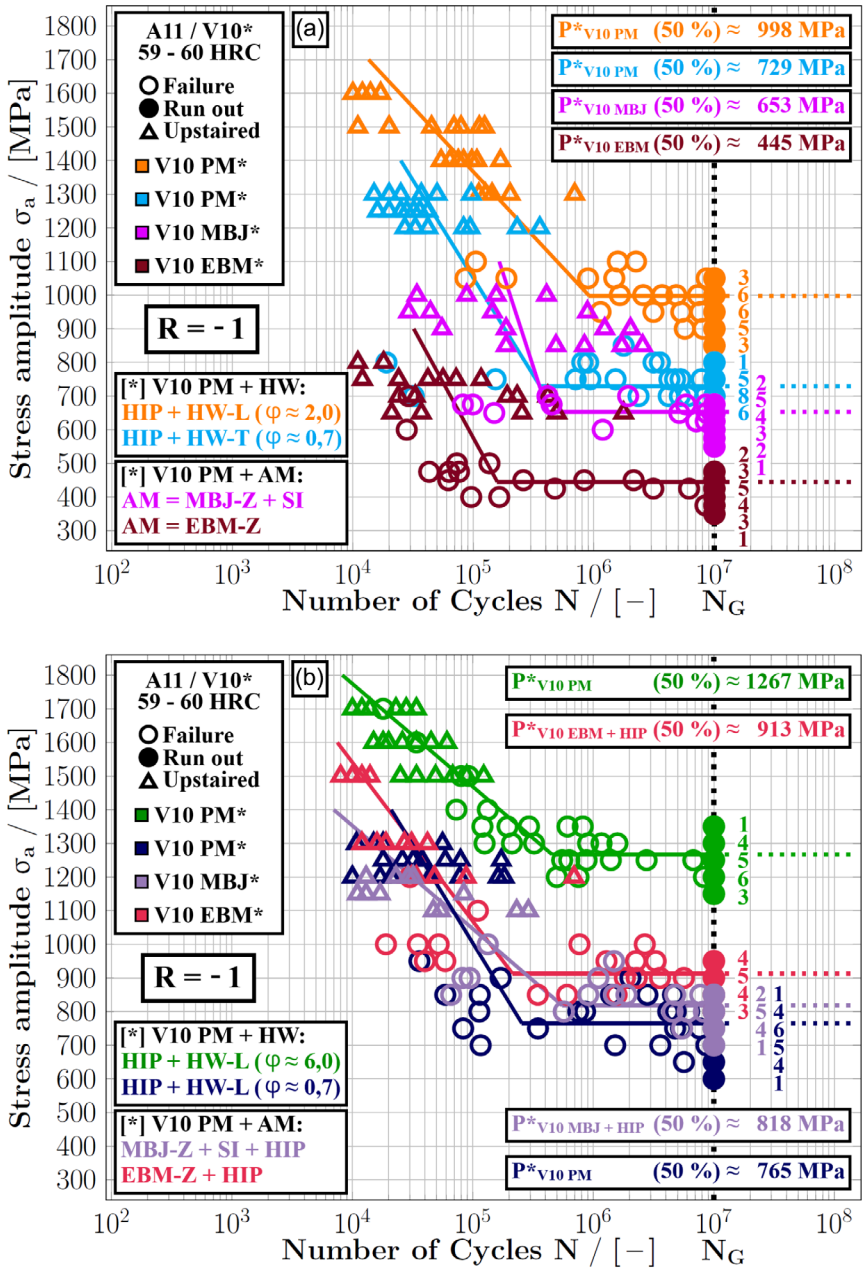


FIGURE 6 | Experimental fatigue data of studied A11 steels and statistically evaluated, "standard" S-N curves for $\sigma_{A,P=50\%}$: (a) PM-L^2, PM-T^1, MBJ-Z, EBM-Z, and (b) PM-L^3, PM-L^1, MBJ-Z + HIP, EBM-Z + HIP.

nonmetallic inclusions (NMI) both clustered with MC (see Figure 5c,d), for PM-L^1/-T^1 large NMI sometimes agglomerated with MC and MnS (see Figure 5e–h), for EBM-Z + HIP only MC (TiC/WC) and NMI or agglomerates from both (see Figure 5i,j), for MBJ-Z only NMI or coarsened MC (see Figure 5k,l), and for PM-L^2 and PM-L^3 only NMI or MC clusters (see Figure 5m–p). From the SFSA fatigue and defect database, the depicted are derived.

Figure 7 compares the statistical, manufacturing-related distributions of geometrical defect properties in A11 microstructures. Figure 8 illustrates the chemical composition of the defects. In this evaluation, all fracture surfaces were chemically analyzed, and the frequency of the various defect types was quantified. In Figure 9, "normalized" S-N curves acc Murakami [13, 27] with fit accuracies (R^2 values) are derived and compared for all eight A11 grades (± 10% error is the model accuracy for $\sigma_{W,Murakami}$).

In Figure 10, a PSPP correlation for fractures/run outs of all A11 grades is developed as the dependence of bearable local stress at defects (σ_L) on the corresponding critical defect size $\sqrt{area}$. Figure 11 illustrates a PSPP correlation for A11 as LLF strength $\sigma_{A,P=50\%}$ over the powder particle size diameter $D_{50\%}$ and HW degree φ, where the effects from HIP and cleaner steel manufacturing/powder handling are indicated (corresponding red boxes and arrows, see Figure 11).

4 | Discussion

The SFSA results presented in Figure 7 explain the achieved fatigue performances and LLF strengths from the A11 grades shown in Figure 4 and Table 4. The conventional grades

1869344x, 0, Downloaded from https://onlinelibrary.wiley.com/doi/10.1002/srin.202500658 by Universitatsbibliothek RWTH Aachen University, Wiley Online Library on [08/05/2026]. See the Terms and Conditions (https://onlinelibrary.wiley.com/terms-and-conditions) on Wiley Online Library for rules of use; OA articles are governed by the applicable Creative Commons License

TABLE 4 | Statistical fatigue strength $\sigma_{A,P}$ [MPa] for RBT at $N_{Grenz} = 10^7$ cycles of the studied steels dependent on the corresponding failure probability P [%], evaluation with in-house SAFD 5 software.

Steel A11	Fatigue strength $\sigma_{A,P}$, MPa for RBT							Scatter band	
	σ_A, $p = 1\%$	σ_A, $p = 5\%$	σ_A, $p = 10\%$	σ_A, $p = 50\%$	σ_A, $p = 90\%$	σ_A, $p = 95\%$	σ_A, $p = 99\%$	Abs., MPa	Rel., %
EBM-Z	239	299	332	445	559	591	652	207	46.4
EBM-Z + HIP	643	722	765	913	1062	1104	1184	271	29.6
MBJ-Z	519	558	579	653	726	747	787	134	20.5
MBJ-Z + HIP	650	699	726	818	911	937	986	168	20.5
PM + HIP-L^1	452	544	593	765	937	986	1077	313	40.8
PM + HIP-T^1	471	547	587	729	872	912	988	259	35.5
PM + HIP-L^2	633	740	797	998	1199	1256	1363	365	36.6
PM + HIP-L^3	947	1041	1091	1267	1443	1493	1587	320	25.3

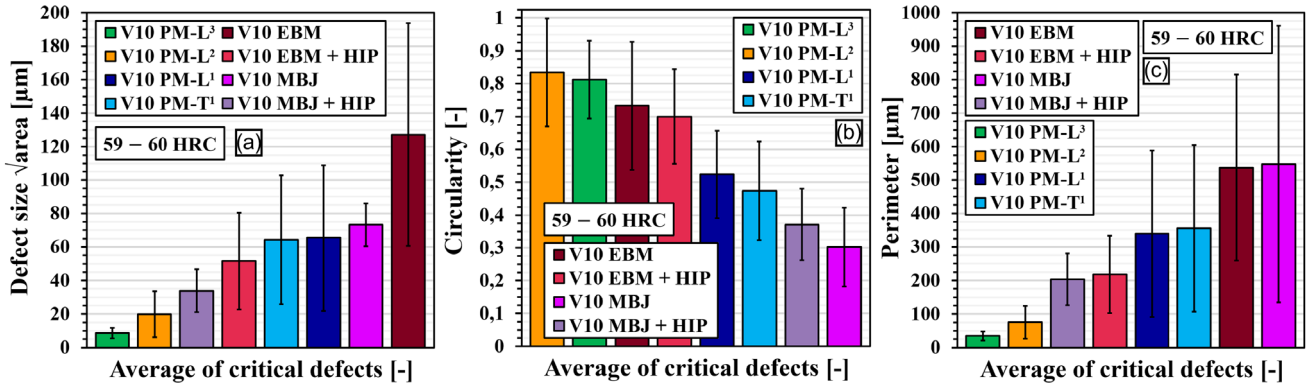


FIGURE 7 | Comparison of geometrical defect properties from SFSA: (a) size $\sqrt{area}$, (b) circularity, and c) perimeter.

PM-L^3 and PM-L^2 achieve higher $\sigma_{A,P=50\%}$ values, because the sizes $\sqrt{area}$ of critical defects in their microstructures is significantly smaller (see Figure 7a,c). In addition, their defects are more circular (see Figure 7b). EBM-Z + HIP and MBJ-Z + HIP achieve slightly higher $\sigma_{A,P=50\%}$ values than the conventional PM-L^1/-T^1 as their relevant defect sizes $\sqrt{area}$ are changed by applying HIP (defect types shifted from larger LoF/porosities to smaller NMI/coarsened MC). Applying HIP onto AM fatigue samples provokes a change in fatigue/failure mechanisms.

The fact that MBJ-Z + HIP shows slightly smaller statistical defect size/scatter than EBM-Z + HIP, but achieves only a slightly smaller $\sigma_{A,P=50\%}$ value (see Figure 6a,b), might be related to statistics and specimen amounts (defect perimeters in Figure 7c are quite similar) or the noticeably less circular defect shapes (see Figure 7b).

The SFSA shows that AM samples without HIP contain larger defects, directly contributing to lower $\sigma_{A,P=50\%}$ values. MBJ-Z without HIP obtains superior fatigue performance and a higher $\sigma_{A,P=50\%}$ value compared to EBM-Z without HIP, because the generated micro cavities clustered with coarsened MC carbides are still remarkably smaller with less size scatter (lesser $\sqrt{area}$ and standard deviation in Figure 7a) than the large LoF/porosities generated by the EBM process. This indicates that AM of CWS has a substantial impact on their carbides (sizes, shapes) and microstructure (defect types/properties), thus on the resulting mechanical properties. Although, EBM creates a more suitable, fine-dispersed and more homogeneous carbide structure (see Figures 1 and 3) than MBJ, due to its faster cooling rates, the generation of more and larger porosity strongly decreases achievable fatigue strengths. Beyond defect size and morphology, the increased carbon contents in the AM conditions are expected to influence both densification kinetics during sintering or HIP and the subsequent microstructure evolution. In MBJ, additional carbon introduced by the organic binder can enhance the local carbon activity during furnace sintering, which may promote the formation and coarsening of primary MC carbides and alter the balance between pore closure and grain growth. Similarly, slightly elevated carbon levels in the EBM condition can shift the equilibrium between matrix and carbide fractions during solidification and post-HIP heat treatment, thereby affecting the spatial distribution and stability of MC particles. These compositional effects are consistent with the pronounced carbide coarsening observed in the MBJ conditions and may contribute, together with the AM-specific defect population, to the increased scatter in fatigue strength and to the prevalence of carbide-assisted crack initiation under HCF loading. Although the present data do not allow for a quantitative separation of compositional and defect-size effects, these considerations suggest that controlling carbon pick-up during AM processing and post-treatments will be

1869344x, 0, Downloaded from https://onlinelibrary.wiley.com/doi/10.1002/srin.202500658 by Universitatsbibliothek RWTH Aachen University, Wiley Online Library on [08/05/2026]. See the Terms and Conditions (https://onlinelibrary.wiley.com/terms-and-conditions) on Wiley Online Library for rules of use; OA articles are governed by the applicable Creative Commons License

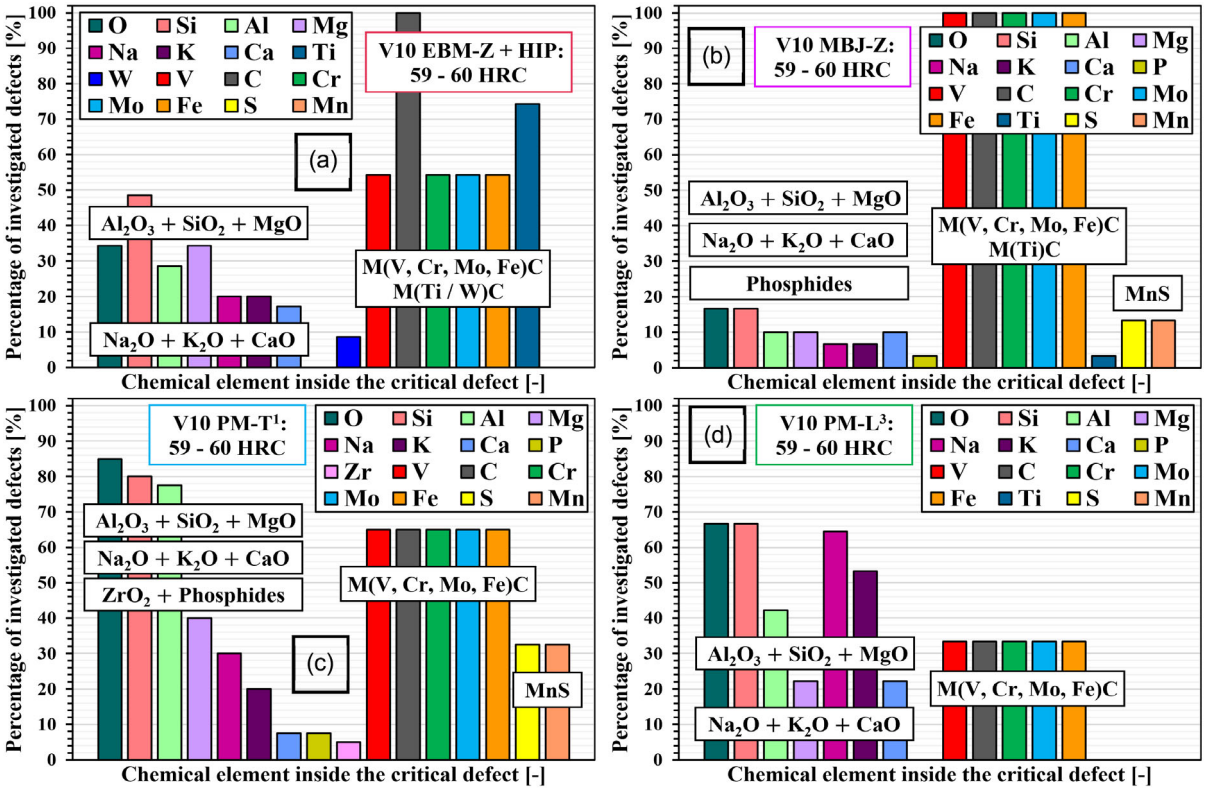


FIGURE 8 | Comparison of the chemical composition of critical defects identified by SFSA based on EDS analysis for selected manufacturing routes: (a) EBM-Z + HIP, (b) MBJ-Z, (c) PM-T^1, and (d) PM-L^3 at a hardness level of 59–60 HRC. The percentage of investigated critical defects containing specific chemical elements is shown, enabling phase attribution to oxide-, carbide-, sulfide-, and phosphide-based inclusions. Corresponding data for additional manufacturing routes and post-treatments are provided in the Supporting Information (Figures S12–S18). The underlying EDS spectra serving as raw data for the elemental evaluation are shown in the Supporting Information (Figures S1–S11).

important for further optimizing the fatigue performance of high-carbon, carbide-rich tool steels.

Therefore, if HIP is not applicable for wear-resistant tools or components, MBJ seems more suitable for CWS and AM toolmaking than EBM. Another advantage of MBJ compared to EBM is the process-related, strongly reduced fatigue and defect size scattering (see Table 4 and Figure 7a). AM porosity problems (in absence of HIP) are also reported by several authors [8–13, 18] and can only be dealt with by parameter/scan optimization or follow-up HIP.

Noteworthy, there is also a strong difference in fatigue strengths and scatter for the conventional A11 grades (see Table 4, Figures 6 and 7), that is directly correlated to microstructural defect properties (mainly size $\sqrt{\text{area}}$), and thus to manufacturing parameters. Low powder cleanliness and reduced φ lead to many larger, more harmful NMI in PM-L^1/-T^1, and thus strongly reduced LLF strength/$\sigma_{A,P=50\%}$ values. Due to high C and V contents in A11 (high MC content) high cleanliness during powder atomization and abstaining further melt sulfurization is even more important, because large NMI can act like foreign surfaces and provoke heterogenous nucleation, intensified (MC) grain growth, and carbide coarsening, which amplifies defect agglomeration mechanisms (NMI + MC + MnS) and increases the intrinsic defect sizes. In addition, chemical analysis of the defects provides further insight. For instance, PM-L^3 exhibits the highest purity and fatigue strength as no sulfur is detected (see Figure 8d), and the defect types occur separately without agglomeration of NMI and MC. In contrast, PM-T^1 shows MnS in ≈ 30% of the cases (see Figure 8c). Furthermore, traces of Zr were also detected, most likely due to wear of the nozzles during the atomization process, as the nozzles are made of ZrO_2. Finally, phosphorus is also noteworthy since the crucibles are repaired with a binder composed of Al_2O_3 and MgO combined with polyphosphoric acid. A portion of this binder is incorporated into the melt and forms phosphides.

The reason for almost negligible anisotropy in PM-L^1/-T^1 is probably the reduced φ and the HW type used (open-die forging has material flow in L and T directions). PM-L^3 and PM-L^2 show outstanding fatigue performance, because their harmful defects (small NMI, MC clusters) are significantly smaller and rounder than those in PM-L^1/-T^1 and inside the AM steels.

This also results when focusing on the scatter (see Table 4). Largest relative scatter bands are exhibited by EBM-Z and PM-L^1, which also show largest scattering of defect sizes $\sqrt{\text{area}}$ (see Table 4 and Figure 7a). The PSPP correlations in Figure 9 clearly demonstrate that the tolerable local stress at a critical defect (σ_L) inside A11 microstructures is directly correlated to the defect size $\sqrt{\text{area}}$ and can be satisfactorily described by power law functions.

Figure 9 also indicates that fatigue performance does not primarily depend on chemical alloy or powder composition, but rather on how the steel microstructure is manufactured. It is important to note that EBM and MBJ represent different manufacturing processes, which influence the effects of particle size on fatigue performance. In Figure 9a, the PSPP correlation demonstrates that powder particle size is significant for both AM and HIP

1869344x, 0, Downloaded from https://onlinelibrary.wiley.com/doi/10.1002/srin.202500658 by Universitatsbibliothek RWTH Aachen University, Wiley Online Library on [08/05/2026]. See the Terms and Conditions (https://onlinelibrary.wiley.com/terms-and-conditions) on Wiley Online Library for rules of use; OA articles are governed by the applicable Creative Commons License

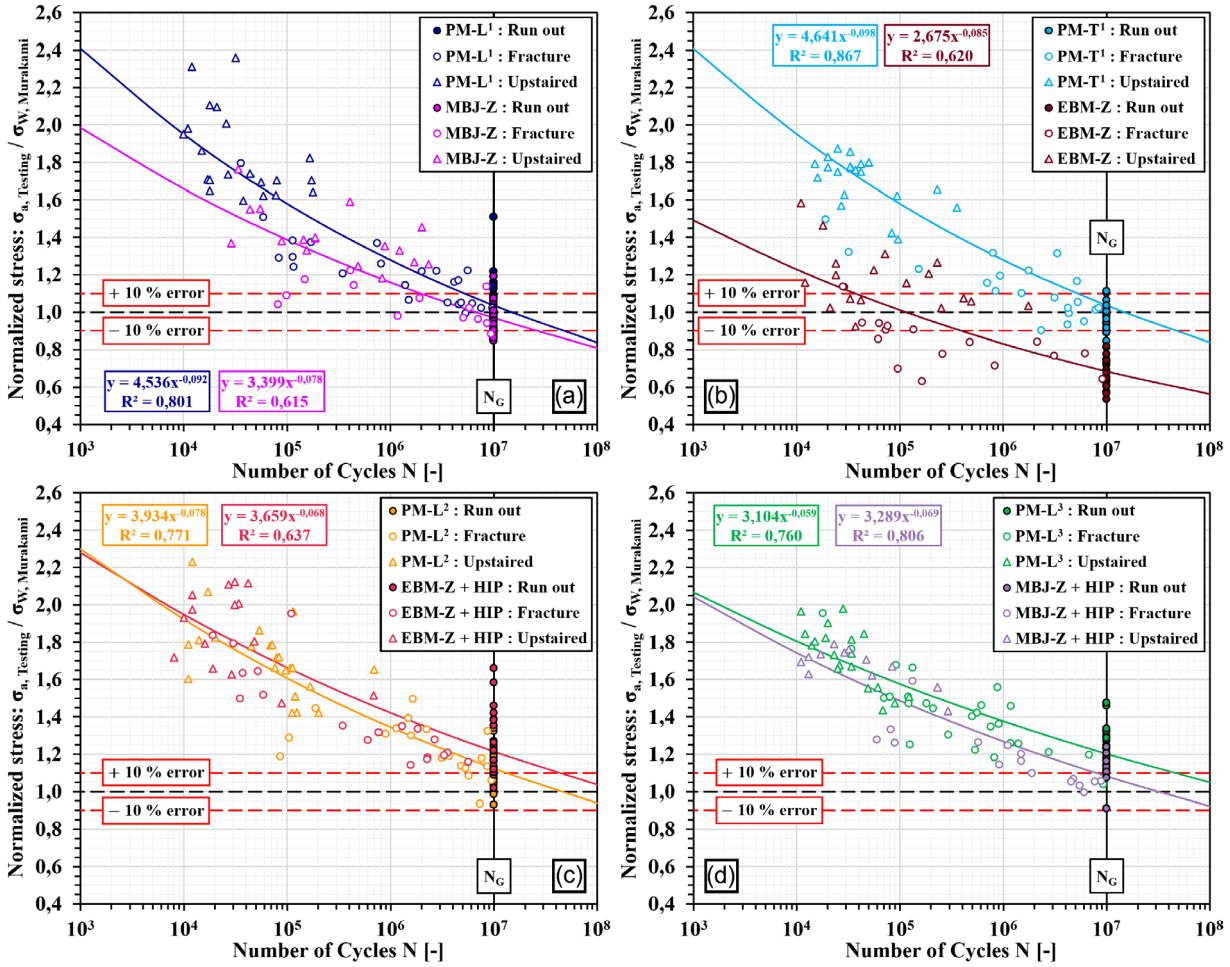


FIGURE 9 | "Normalized" S-N curves developed by combining exp. fatigue and SFSA defect data for: (a) PM-L[1] and MBJ-Z, (b) PM-T2 and EBM-Z, (c) PM-L2 and EBM-Z + HIP, and (d) PM-L3 and MBJ-Z + HIP.

powders; specifically, the maximum particle size achieved by sieving limits the sizes of defects such as NMI and coarsened MC clusters in steel powders. However, in EBM, the full melting process may reduce the impact of particle size on fatigue life. Additionally, argon atomized coarse particles can contain internal pores that lead to persistent porosity in EBM components due to argon's insolubility in the matrix. Future studies could benefit from varying particle sizes within PM-HIP processes to further understand their influences on fatigue life. In the EBM-Z + HIP grade, trace amounts of tungsten and a relatively high titanium content are detected. One possible explanation for this elevated titanium level is that titanium-bearing compounds like ferrotitanite might have been processed during atomization and left residues behind, or that titanium is intentionally added to reduce oxygen content in the steel. A similarly low titanium level in the MBJ-Z grade suggests mutual solubility among these MCs (see Figure 8b). The MCs present in A11 powder grains likely originate from suboptimal powder handling or alternative containers and adversely affect fatigue strength and crack initiation; intentional additions of TiC and WC for enhancing wear resistance in MMC-like steels must be excluded here. Furthermore, the negligible fraction of non-metallic inclusions found in MBJ-Z is not due to superior powder purity but rather a consequence of pronounced coarsening of matrix carbides.

In Figure 11a, it is indicated that $\sigma_{A,P=50\%}$ improvement for conventional A11 grades is more related to cleanliness and φ than to positive effects from decreased powder particle size $D_{50\%}$. Therefore, Figure 11b shows the PSPP correlation over φ. For $\sigma_{A,P=50\%}$ of the AM steels the shifting effect obviously comes from HIP because it holds $\varphi = 0$ for EBM and MBJ processes.

But for conventional steels a strong dependence of $\sigma_{A,P=50\%}$ on φ and steel cleanliness results. If φ or a cleaner atomization/powder handling is the most relevant process factor for conventional A11 grades, is not distinguishable based on the presented study/results.

The 'normalized' S-N curves presented in Figure 9 demonstrate the correlation between intrinsic defect sizes ($\sqrt{area}$), steel hardness (HV), number of cycles to failure (N) and tolerable, local stress level (σ_L or σ_N) for A11. By applying normalization onto standard S-N curves, steel hardness and critical defect data can be included into the visualization.

As explained by Murakami [13, 27], this enables a better assessment and comparison of fatigue scatter, test machine alignments, or influences from AM and different defect sizes. If the normalized data points for fractures in Figure 9 are around or above $\sigma_N \approx 0.9 - 1.1$ (model error/accuracy band) they are well predicted by the model [15] and the test machines are well aligned (absence of possible superimposed bending stresses during

1869344x, 0, Downloaded from https://onlinelibrary.wiley.com/doi/10.1002/srin.202500658 by Universitatsbibliothek RWTH Aachen University, Wiley Online Library on [08/05/2026]. See the Terms and Conditions (https://onlinelibrary.wiley.com/terms-and-conditions) on Wiley Online Library for rules of use; OA articles are governed by the applicable Creative Commons License

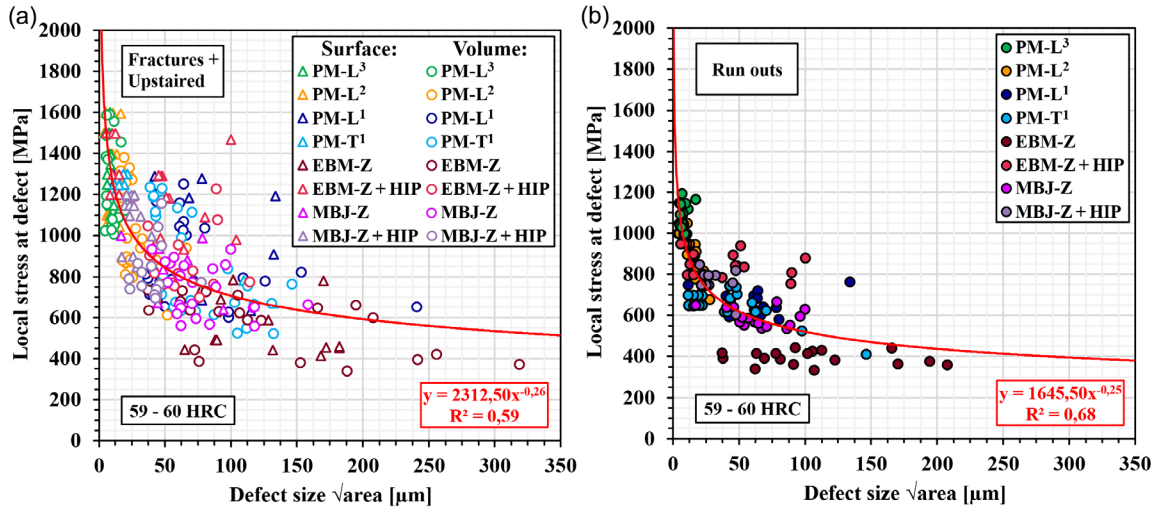


FIGURE 10 | PSPP correlation for A11 as local stress (σ_L) over the defect size $\sqrt{area}$ for: (a) fractures, (b) run outs.

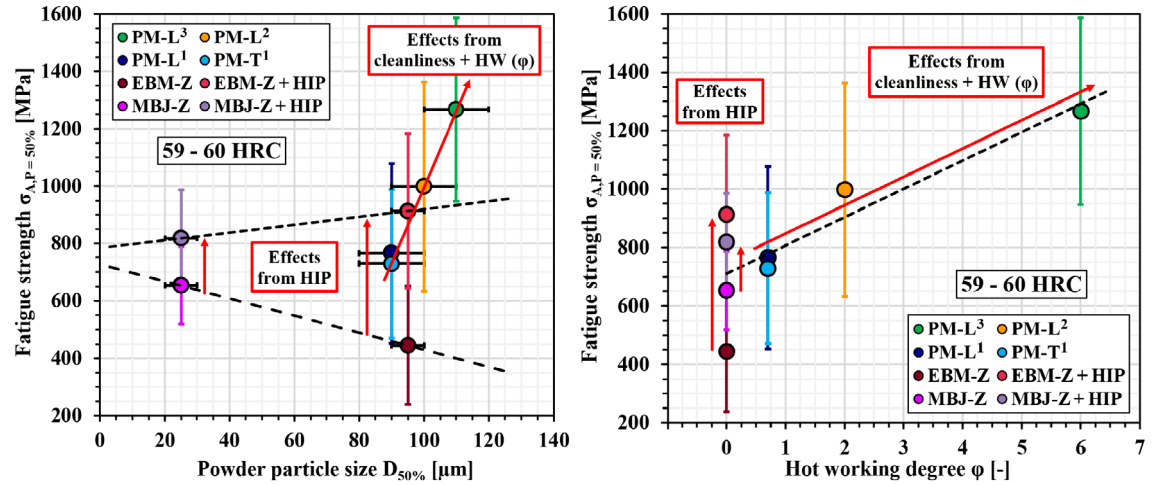


FIGURE 11 | PSPP correlation for A11 as $\sigma_{A,P=50\%}$ over the powder particle size diameter $D_{50\%}$ and the HW degree φ.

fatigue testing). If the normalized data points for run outs in Figure 9 are around or below $\sigma_N \approx 0.9-1.1$ they are well predicted and interferences with, e.g., relevant surface-near RS or high surface roughness, can probably be excluded (is negligible).

In Figures 9a and 8b, the large scatter of fatigue data from PM-L^1/-T^1 and EBM-Z can be reduced efficiently by applying normalization (similar for PM-L^3 and MBJ-Z + HIP in Figure 9d). All fractures in Figure 9, excepted EBM-Z, are inside or above the model error band, which means they are well predicted and test machines are well aligned. Noteworthy, many of the run outs from PM-L^1, PM-L^2, PM-L^3, EBM-Z + HIP, and MBJ-Z + HIP are slightly or heavily above the error band, indicating the presence of relevant surface-near, compressive residual stresses (CRS) inside the fatigue specimens from sample fabrication (hard turning and/or polishing).

In Figure 9, fabrication-induced CRS can shift run outs further upward, whereby the effect seems less or negligible for PM-L^1/-T^1, MBJ-Z, and EBM-Z (but same sample fabrication and finishing for all batches). It can be assumed that effects from CRS are also dependent on defect size, amount, and localization. A noticeable shifting effect can only be seen for steels with rather smaller defects (PM-L^2, PM-L^3, EBM-Z/MBJ-Z + HIP, see Figure 9). Negligible shifting effect arises for steels with rather larger defects (PM-L^1/-T^1, MBJ-Z, EBM-Z, see Figure 9), even though the present CRS are probably quite similar in all batches.

Some fractures from EBM-Z samples containing large defects (mostly volume), and all run outs in Figure 9b are clearly below the error band, indicating poor model suitability (and are contradictory to suspected CRS effects and well aligned test machines). This sometimes for AM metals without HIP appearing behavior was also recently reported by Murakami [13] and might be related to facilitated crack forming/density problems, close to each other located defect interactions or inconsistency with the basic fracture mechanical and physical model assumptions.

While this study does not currently analyze the complementary effects of defect chemistry on fatigue performance, it is recognized as a valuable area for future research. Investigating how different chemical compositions of defects influence bonding strength and failure mechanisms could provide deeper insights into fatigue behavior. Such studies may help explain some of the deviations observed in this work and further refine predictive models for fatigue life in advanced tool steels.

1869344x, 0, Downloaded from https://onlinelibrary.wiley.com/doi/10.1002/srin.202500658 by Universitatsbibliothek RWTH Aachen University, Wiley Online Library on [08/05/2026]. See the Terms and Conditions (https://onlinelibrary.wiley.com/terms-and-conditions) on Wiley Online Library for rules of use; OA articles are governed by the applicable Creative Commons License

5 | Conclusion

This study demonstrates the feasibility of processing high-carbon, carbide-rich CWS via AM using EBM and MBJ. Establishing additive toolmaking as viable methods for conventional tool applications requires a profound understanding of the relationships within the PSPP chain. Eight differently manufactured A11 grades were statistically fatigue tested under RBT, their microstructures/critical defect populations were characterized quantitatively via SFSA to finally develop statistical PSPP correlations and normalized S-N curves for A11.

AM without HIP only exhibits strongly decreased LLF strengths compared to conventional steelmaking via PM + HIP. Significant strength increase is observed when applying HIP after AM, which could be particularly beneficial in critical or exceptional tooling applications. For PM + HIP steels powder cleanliness and carbide sizes remain most essential (avoiding all coarsening and clustering). The manufacturing technique (including powder cleanliness, grain size distribution, powder sieving, HIP application, and HW degree φ) is most crucial for HCF strength because it determines steel microstructure/carbide structure and their critical defect properties (size, shape, amount, spatial distribution, clustering/agglomeration phenomena).

The outstanding, primary influencing factor for LLF is the defect size $\sqrt{\text{area}}$, which has to be controlled during steelmaking or AM toolmaking to achieve superior fatigue performances.

Overall, the results highlight the complex relationships inside PSPP chains of high-performance steels like A11. Targeted steel characterization and controlling along the PSPP chain is the appropriate key to optimize material, component or tool performances. Herein, the SFSA method acc Scholl et al. [22–26] is a very suitable, scientific working tool that enables comparable statistical data collection and quantitative assessments of critical defects. Future work should focus on optimization potentials and practical, efficient enhancements of AM processing for A11 as well as improving starting powder quality via cleaner atomization and handling.

Author Contributions

Frederik Tegeder: conceptualization (lead); data curation (lead); formal analysis (lead); investigation (lead); methodology (lead); project administration (lead); supervision (lead); writing – original draft (lead); writing – review & editing (lead). **Lennart Mirko Scholl**: visualization (lead); writing – review & editing (lead). **Sandra Wieland**: data curation (equal). **Christian Weck**: data curation (equal). **Marie Franke-Jurisch**: data curation (equal). **Alexander Bezold**: writing – review & editing (supporting). **Thomas Weißgärber**: supervision (supporting). **Christoph Broeckmann**: supervision (lead).

Acknowledgments

The authors greatly appreciate the substantial support from Prof. Dr.-Ing. C. Escher/Dipl.-Ing. M. Tradt (Dörrenberg), Dr.-Ing. A. Barani (ZAPP), Dr.-Ing. G. Walkowiak/Dipl.-Ing. U. Schwahn (Bodycote Esslingen), Dipl.-Ing. A. Arany (Kutz & Schulze), and Dr.-Ing. H. Hill/M. Sc. J. Conrads/M. Sc. P. Kluge (DEW Krefeld) for material/powder supplies, heat treatments with hardness testing, and thorough discussions during the investigations.

Open Access funding enabled and organized by Projekt DEAL.

Funding

This work was supported by research projects IGF-No. 01IF22271N/FOSTA P 1608 from the "'Research Association for Steel Application e.V.'" (FOSTA), Düsseldorf, Germany and IGF-No. 01IF22507N from the "'Research Association for Steel Forming e.V.'" (FSV), Hagen, Germany, were supported by the Federal Ministry for Economic Affairs and Climate Action (BMWK) through the project management sponsor/Projektträger "'Deutsches Zentrum für Luft- und Raumfahrt e.V.'" (DLR), Bonn, Germany, as part of the program for promoting industrial cooperative research (IGF) on the basis of a decision by the German Bundestag.

Conflicts of Interest

The authors declare no conflicts of interest.

Data Availability Statement

The data that support the findings of this study are available from the corresponding author upon reasonable request.

References

1. W. Reiss, *VDI-Zeitschrift* 130, 1 (1988): 56–62.

2. I. Jung, Ermüdungsfestigkeit Hochlegierter Werkzeugstähle, *Journal of Heat Treatment and Materials* 65 (2010): 278–284.

3. G. Jesner, *Dissertation Thesis*. Montanuniversität Leoben, 2007, Austria.

4. I. Gibson, D. W. Rosen, and B. Stucker, *Additive Manufacturing Technologies: 3D Printing, Rapid Prototyping, and Direct Digital Manufacturing* (Springer, 2015), https://doi.org/10.1007/978-1-4939-2113-3.

5. D. Herzog, V. Seyda, E. Wycisk, and C. Emmelmann, "Additive Manufacturing of Metals," *Acta Materialia* 117 (2016): 371–392, https://doi.org/10.1016/j.actamat.2016.07.019.

6. M. J. Bermingham, D. Kent, H. Zhan, D. H. StJohn, and M. S. Dargusch, "New Developments in Metal Additive Manufacturing: A Review of Processes, Properties and Applications," *Journal of Materials Science & Technology* 34, no. 1 (2018): 102–640, https://doi.org/10.1016/j.jmst.2017.11.015.

7. F. Klocke, K. Arntz, N. W. Klingbeil, et al., "Additive Manufacturing in Production Engineering – New Possibilities for Toolmaking and Lightweight Construction," *CIRP Annals* 66, no. 2 (2017): 561–583, https://doi.org/10.1016/j.cirp.2017.05.009.

8. N. Sanaei and A. Fatemi, "Defects in Additive Manufactured Metals and Their Effect on Fatigue Performance: A State-of-the-Art Review," *Progress in Materials Science* 117 (2021): 100724, https://doi.org/10.1016/j.pmatsci.2020.100724.

9. J. Kunz, M. L. Köhler, and S. Herzog, "Influence of an Increasing Alloying Content on the Microstructure of a High-Speed Steel in the Laser-Powder Bed Fusion Process," *Steel Research International* 92 (2021): 12, https://doi.org/10.1002/srin.202100438.

10. J. Kunz, J. Saewe, and S. Herzog, "Mechanical Properties of High-Speed Steel AISI M50 Produced by Laser Powder Bed Fusion," *Steel Research International* 91, no. 5 (2020): 1900562, https://doi.org/10.1002/srin.201900562.

11. J. Kunz, S. Herzog, and A. Kaletsch, "Influence of Initial Defect Density on Mechanical Properties of AISI H13 Hot-Work Tool Steel Produced by Laser Powder Bed Fusion and Hot Isostatic Pressing," *Powder Metallurgy* 65 (2022): 1, https://doi.org/10.1080/00325899.2021.1934634.

12. K. Kempen, B. Vrancken, and S. Buls, "Selective Laser Melting of Crack-Free High Density M2 High Speed Steel Parts by Baseplate

1869344x, 0, Downloaded from https://onlinelibrary.wiley.com/doi/10.1002/srin.202500658 by Universitatsbibliothek RWTH Aachen University, Wiley Online Library on [08/05/2026]. See the Terms and Conditions (https://onlinelibrary.wiley.com/terms-and-conditions) on Wiley Online Library for rules of use; OA articles are governed by the applicable Creative Commons License

Preheating," *Journal of Manufacturing Science and Engineering* 136, no. 6 (2014): 061026, https://doi.org/10.1115/1.4028513.

13. Y. Murakami, T. Takagi, and K. Wada, "Essential Structure of S-N Curve: Prediction of Fatigue Life and Fatigue Limit of Defective Materials and Nature of Scatter," *International Journal of Fatigue* 146 (2021): 106138, https://doi.org/10.1016/j.ijfatigue.2020.106138.

14. D. Godlinski and G. Veltl, "Rapid Manufactured Complex PMİTool Steel Parts," *Proceedings of 16th Int. Plansee Seminar*, 2005, 82–96.

15. V. Friederici and S. Wieland, "Laser Beam Melting of Heat Treatable 56NiCrMoV7 and Wea-Resistant FeCrV10 Steel," *Proceedings of EuroPM*, 2017, 131–138.

16. M. Ziaee and N. B. Crane, "Binder Jetting: A Review of Process, Materials, and Methods," *Additive Manufacturing* 28 (2019): 781–801, https://doi.org/10.1016/j.addma.2019.05.031.

17. M. Li, W. Du, and A. Elwany, "Metal Binder Jetting Additive Manufacturing: A Literature Review," *Journal of Manufacturing Science and Engineering* 142, no. 9 (2020): 090801, https://doi.org/10.1115/1.4047430.

18. M. Franke-Jurisch, M. Mirz, and T. Wenz, "PBF-EB of Fe-Cr-V Alloy for Wear Applications," *Materials* 15, no. 5 (2022): 1679, https://doi.org/10.3390/ma15051679.

19. F. Tegeder, S. Wieland and J.Eckel, "Processing of Ledeburitic Cold Work Tool Steel A11 Using Metal Binder Jetting," *Proceedings of EuroPM*, 2024, 216–222, https://doi.org/10.59499/EP246281685.

20. DIN eV, *Umlaufbiegeversuch* (Beuth GmbH, 2018).

21. DIN eV: 50100:2022-12, *Schwingfestigkeitsversuch* (Beuth GmbH, 2022).

22. L. M. Scholl, A. Bezold, and C. Broeckmann, "Influences of Manufacturing-Related Microstructural Variations on Fatigue in Carbide-Rich Tool Steels," *Proceedings of 12th Int. Tooling Conf*, 2022, 244–252.

23. L. M. Scholl, A. Bezold, and C. Broeckmann, "Influence of Plasma Nitriding on the Fatigue Strength of Carbide-Rich Tool Steels," *Proceedings of 12th Int. Tooling Conf*, 2022, 368–376.

24. L. M. Scholl, A. Bezold, and C. Broeckmann, "Influences of Manufacturing-Related Microstructural Variations on Fatigue in Carbide-Rich Tool Steels," *Steel Research International* 94, no. 4 (2023): 2200578, https://doi.org/10.1002/srin.202200578.

25. L. M. Scholl, F. Tegeder, and A. Bezold, "Fatigue-Oriented Design of High-Strength Tools Made of Carbide-Rich PM Tool Steels Under Multiaxial Cyclic Loading," *Proceedings of 6th ESTAD Conf*, 2023.

26. L. M. Scholl, F. Tegeder, and A. Bezold, "Einfluss von Karbidgröße, Reinheitsgrad und Härte auf die Ermüdungsfestigkeit Karbidreicher Kaltarbeitsstähle," *Proceedings of Werstoffprüfung*, 2023, https://doi.org/10.48447/WP-2023-261.

27. Y. Murakami, *Metal Fatigue – Effects of Small Defects* 2nd Ed. (Academic Press, 2019).

Supporting Information

Additional supporting information can be found online in the Supporting Information section.

1869344x, 0, Downloaded from https://onlinelibrary.wiley.com/doi/10.1002/srin.202500658 by Universitatsbibliothek RWTH Aachen University, Wiley Online Library on [08/05/2026]. See the Terms and Conditions (https://onlinelibrary.wiley.com/terms-and-conditions) on Wiley Online Library for rules of use; OA articles are governed by the applicable Creative Commons License